Tribology International 214 (2026) 111352

Contents lists available at ScienceDirect

Tribology International

journal homepage: www.elsevier.com/locate/triboint

Full Length Article

Leakage at interfaces: A comprehensive study based on Persson contact mechanics theory

R. Xu [a,b,c], L. Gil [d], J. Singer [d], L. Gontard [d], W. Leverd [d], B.N.J. Persson [a,b,c,*]

[a] Peter Grünberg Institute (PGI-1), Forschungszentrum Jülich, 52425, Jülich, Germany
[b] State Key Laboratory of Solid Lubrication, Lanzhou Institute of Chemical Physics, Chinese Academy of Sciences, 730000 Lanzhou, China
[c] MultiscaleConsulting, Wolfshovener str. 2, 52428 Jülich, Germany
[d] BD Medical-Pharmaceutical Systems, 11 Rue Aristide-Bergès, Le Pont de Claix 38801, France

ARTICLE INFO

Keywords:
Contact mechanics
Sealing
Leakage prediction
Surface roughness

ABSTRACT

We present a comprehensive study that combines theory and experiments on gas leakage at rubber–glass interfaces in a prototype syringe system. Leakage measurements were conducted under controlled dry conditions and compared with predictions from a new approach that integrates finite element simulations, which neglect microscopic roughness and provide deterministic pressure profiles, with Persson contact mechanics and leakage theory. The latter incorporates the measured random surface roughness, characterized using stylus profilometry and atomic force microscopy, to determine local flow factors with high accuracy. The predicted leakage rates show good agreement with experimental results. Furthermore, sensitivity analyses reveal that small variations in elastic modulus and contact pressure can markedly influence leakage behavior, especially near the percolation threshold. This work establishes a generalized and experimentally validated framework for leakage prediction and provides practical guidance for the design and optimization of sealing systems in pharmaceutical and engineering applications.

1. Introduction

All solid surfaces exhibit roughness. When two nominally flat surfaces come into contact, unless contact pressures are very high or at least one of the two solids in contact is very soft, non-contact areas will always exist at the interface, leading to interfacial separation (gaps) between the solids. When the non-contact areas percolate, the gaps extend from one side of the nominal contact zone to the other, resulting in leak paths that allow fluid to flow through the interface.

A seal is a device used to close these gaps, prevent the leakage of fluids or gases, and ensure the proper functioning of mechanical systems. Seals are typically made of elastomeric materials (such as rubber) that can adapt to various shapes and pressure conditions. Common types include O-rings and gaskets. Seal failure can result in environmental pollution, energy loss, and significant engineering failures.

Although sealing is of great importance, predicting leakage for both gases and liquids remains a complex theoretical challenge. The general mechanisms governing leakage are similar, but the two cases differ in their basic assumptions. Liquids are treated as incompressible with constant viscosity, while gases are compressible and their effective conductivity depends on both pressure and the mean molecular velocity. These differences are reflected in the continuity and flow equations discussed later in the theory section. In the present study, we focus on gas leakage experiments for validation, but the same theoretical approach can also be applied to liquid leakage problems by adopting the corresponding viscosity law. Understanding these distinctions is essential for accurate modeling and prediction of leakage under different operating conditions.

At the same time, the characteristics of the leak path are strongly influenced by the interfacial separation, which in turn depends on surface roughness. Solid surfaces exhibit roughness over many decades of length scales [1–3], with common engineering surfaces displaying roughness spanning lengths from centimeters to nanometers. This multiscale nature of roughness complicates investigations using deterministic simulation methods.

One approach to addressing the problem of interfacial surface separation under a given pressure is to use contact mechanics theories. Two main families of theories are used to study the contact of rough solids: the Greenwood-Williamson (GW) theory [4] and the Persson theory [5–10].

The GW theory approximates the roughness of a real surface as a series of spherical caps with random heights. The contact of each asperity is determined using Hertz theory, and from this, the total

* Corresponding author at: Peter Grünberg Institute (PGI-1), Forschungszentrum Jülich, 52425, Jülich, Germany.
E-mail address: b.persson@fz-juelich.de (B.N.J. Persson).

https://doi.org/10.1016/j.triboint.2025.111352
Received 13 July 2025; Received in revised form 22 October 2025; Accepted 26 October 2025
Available online 30 October 2025

number of contact regions, total contact area, and surface separation at a given load can be derived. The GW theory is widely used, particularly by engineers, due to its simplicity. However, it relies on several assumptions: independent spherical asperities with identical radii and a random distribution of heights. These assumptions neglect (i) the multiscale nature of real surface roughness and, most importantly, (ii) the long-range elastic deformation: when one asperity deforms, neighboring asperities around it also deform. This effect is critical in calculating leakage paths [11]. Although refinements to the GW model, such as the Bush, Gibson, and Thomas (BGT) model [12] and the Chang, Etsion, and Bogy (CEB) model [13], have been developed to address these limitations, these theories are generally considered suitable only for small loads [14]. Due to these inherent limitations, particularly the neglect of elastic coupling and multiscale roughness, the GW model has been proven not suitable for leakage analysis, as it cannot reliably predict surface separation and the size of leak paths [11,15].

The Persson theory discards the assumption of a small real contact area relative to the nominal contact area and instead begins with the case of complete contact [5,10]. The central idea is that at low magnification ζ, the true contact area A equals the nominal contact area A_0. Here, A and A_0 refer to the projections of the actual and nominal contact regions on the horizontal xy plane. However, as the magnification increases, non-contact areas (due to surface roughness) become visible. The Persson theory can be used to calculate various contact properties, such as the relative contact area A/A_0 and the probability distribution of interfacial separation $P(u)$, which is used in the theory for leakage.

While the Persson theory is exact under full contact conditions [14], it also provides accurate estimations at small contact pressures [10, 11], enabling reliable leakage predictions in contacts [15–17]. Dapp and Müser further demonstrated [18] that the Persson theory based on Bruggeman effective medium approach remains valid even near the percolation threshold, where leakage is dominated by a single critical constriction. These findings confirm the accuracy and broad applicability of the theory.

Leakage prediction using the Persson theory requires the surface roughness power spectral density (calculated from measured surface topography) and information about the contact as input. This includes the elastic (or elastoplastic) properties of the solids, properties of the fluids, contact pressure, and fluid pressure (or pressure difference). In recent years, numerous practical studies have applied the Persson contact mechanics theory to investigate leakage and sealing. These include research on static metallic seals [19–21], elastomer seals [22–26], metallic ball valves [27], dynamic seals [28–30], and leakage in face masks [31].

The current state of the art in using the Persson contact mechanics theory to study leakage and sealing problems is as follows:

(i) Leakage predictions considering surface roughness [16].
(ii) Leakage predictions using different separation theories (critical junction and effective medium) [32,33].
(iii) Leakage of fluids in different flow regimes, diffusive or ballistic (gas) [26].
(iv) Leakage with fluid-pressure-induced surface deformation [34].
(v) Influence of plastic deformation on the leak rate (in an approximate way) [19,20].
(vi) Role of hydrophobicity on the leak rate [35].

Although these studies have addressed many aspects, a common limitation is the assumption that the pressure distribution in the seal is either Hertzian (for O-rings) or rectangular (for gaskets). These assumptions are not accurate in many practical applications.

The present study focuses on air leakage at rubber–glass interfaces in a prototype syringe system consisting of a rubber stopper and a glass barrel supplied by Becton Dickinson (BD) Medical-Pharmaceutical Systems. Experiments were performed under controlled dry conditions, and the results were compared with predictions from a new approach that combines numerical finite element method (FEM) calculations, which neglect microscopic roughness and yield deterministic pressure profiles, with Persson contact mechanics theory. All relevant features are implemented in the Multiscale Contact Mechanics (MCM) software to predict leakage.

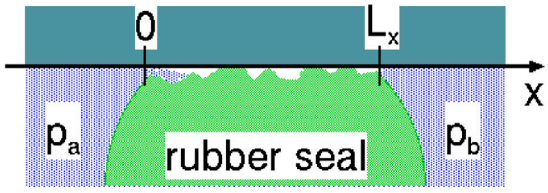

Fig. 1. Cross-section of a circular seal orthogonal to the angular direction. The fluid pressure $p_a > p_b$ and fluid leakage occurs along the positive x-axis.

In the system studied, the separation at the critical constriction u_c is much smaller than the gas molecule mean free path λ, and gas leakage therefore occurs in the ballistic limit (see Ref. [26]). In Ref. [26], leakage was analyzed by scaling the leak rate in the diffusive limit by a factor proportional to λ/u_c to estimate leakage in the ballistic regime. In contrast, the present study employs leak rates derived rigorously for the ballistic limit, as detailed in the theory section and Appendix A, within a unified theoretical framework developed for both incompressible liquids and compressible gases.

The predicted gas leak rates show good agreement with experimental measurements. Furthermore, the simulations reveal that small variations in elastic modulus E and nominal contact pressure p_0 can significantly affect leakage, particularly near the percolation threshold. These results improve the understanding of how leakage depends on contact conditions and provide useful insights for the design of seals and mechanical systems.

2. Theory

Here we describe the theory used to obtain the leakage rate of fluids in torus-shaped rubber seals with an arbitrary cross section. We calculate the fluid leakage using the effective medium theory developed in Ref. [17] (see also Refs. [32,33,36–39]). Here we review the basic equations.

Consider the flow of a fluid at the interface between two solids with surface roughness. For an incompressible fluid (liquid), the conserved quantity is the volume of fluid, and the continuity equation for fluid flow takes the form

$$\nabla \cdot \mathbf{J}_{\text{liquid}} = \frac{\partial u}{\partial t} \tag{1}$$

where $u(\mathbf{x}, t)$ is the interfacial separation. For a compressible fluid (gas), the conserved quantity is not the volume of fluid but the number of atoms (or molecules). In this case,

$$\nabla \cdot \mathbf{J}_{\text{gas}} = \frac{\partial n}{\partial t} \tag{2}$$

where n is the number of molecules per unit surface area. Note that the two flow currents have different dimensions: m^2/s for the incompressible fluid and $1/\text{s}$ m for the (compressible) gas.

In what follows, we assume stationary conditions so that there is no dependency on time. For an incompressible fluid, the (microscopic) flow current is related to the pressure gradient as follows [33]:

$$\mathbf{J}_{\text{liquid}}(\mathbf{x}) = -\frac{u^3}{12\eta}\nabla p. \tag{3}$$

Here, η is the fluid viscosity and $p(\mathbf{x})$ is the pressure at the lateral point $\mathbf{x} = (x, y)$ at the interface. The pressure is assumed to be independent of the coordinate z, which is normal to the interface. The current $\mathbf{J}_{\text{liquid}}$ represents the volume of fluid per unit surface area multiplied by the

average flow velocity across the thickness of the gap (with units of $m^3/m^2 \times m/s = m^2/s$). For a gas [26]:

$$\mathbf{J}_{\rm gas}(\mathbf{x}) = -\left(\frac{u^3 p}{12 k_{\rm B} T \eta} + \frac{\bar{v} u^2}{2 k_{\rm B} T}\right) \nabla p. \tag{4}$$

Here we assume the temperature is constant. In (4) we interpolate between diffusive airflow (first term) and ballistic airflow (second term), see Ref. [26]. That is, when the separation between the surfaces is much larger than the mean free path of gas molecules, the fluid flow is diffusive. In the opposite limit, there are no collisions between molecules, and they propagate ballistically between collisions with solid walls.

The flow conductivity $\sigma(\mathbf{x})$ is defined by

$$\mathbf{J}_{\rm fluid}(\mathbf{x}) = -\sigma(\mathbf{x}) \nabla p(\mathbf{x})$$

so that

$$\sigma = \frac{u^3}{12\eta} \tag{5}$$

for an incompressible liquid, and

$$\sigma = \frac{u^3 p}{12 k_{\rm B} T \eta} + \frac{\bar{v} u^2}{2 k_{\rm B} T} \tag{6}$$

for a compressible gas. In the study presented below, the surface separation at the critical constriction (the separation between surfaces at the narrowest constrictions along the leak path) varies between ~10–20 nm depending on the gas pressure. The gas molecule mean free path is about ~60 nm. Hence, we are well within the Knudsen limit, where gas molecules move ballistically between collisions with the solid walls, and the second term in (6) dominates. For surfaces with roughness on multiple length scales, $u(\mathbf{x})$, $p(\mathbf{x})$, and $\sigma(\mathbf{x})$ vary rapidly with the spatial coordinate $\mathbf{x}$.

Consider a torus-like seal (see Fig. 1) and let x be the axis along the fluid leakage direction. The seal contacts a smooth surface for $0 < x < L_x$. Assume that the fluid pressure is $p_{\rm a}$ for $x < 0$ and $p_{\rm b} < p_{\rm a}$ for $x > L_x$. In this case, fluid flow occurs in the positive x-direction.

For an incompressible fluid, σ is given by (5) and depends on the spatial coordinate $\mathbf{x}$ only via u. For a compressible gas, σ is given by (6) depends on $u(\mathbf{x})$ *and* the fluid pressure $p(\mathbf{x})$. This makes the problem more complex. To simplify, we replace p in (6) with $(p_{\rm a}+p_{\rm b})/2$, i.e., the average of the fluid pressure between the two sides of the seal region. After this approximation, σ depends on $\mathbf{x}$ only via $u(\mathbf{x})$.

The ensemble-averaged fluid flow current is

$$\mathbf{J} = -\sigma_{\rm eff} \nabla p_{\rm fluid}$$

where $p_{\rm fluid}$ is the ensemble-averaged fluid pressure and $\sigma_{\rm eff}$ is the corresponding effective flow conductivity. Here $\mathbf{J}$, $\sigma_{\rm eff}$, and $p_{\rm fluid}$ vary slowly in space and are obtained from the corresponding microscopic quantities in Eqs. (1)–(6) after averaging out the roughness (ensemble-averaging). Thus, while $\mathbf{J}_{\rm fluid}(\mathbf{x})$ varies rapidly in space due to surface roughness, the ensemble-averaged current $\mathbf{J} = \langle \mathbf{J}_{\rm fluid} \rangle$ represents an effective flow current for a smooth reference interface obtained by coarse-graining the microscopic roughness. This averaged current varies spatially only due to the macroscopic shape of the contact. The averaging is carried out using the Bruggeman effective medium theory (see [15,40], section below, and Appendix A, where an effective flow conductivity $\sigma_{\rm eff}$ is calculated).

The probability distribution of interfacial separation can be written as

$$P(u) = \frac{A}{A_0}\delta(u) + P_{\rm c}(u) \tag{7}$$

where A/A_0 is the relative contact area ($u = 0$ contribution to $P(u)$) and where $\delta(u)$ is the Dirac delta function which vanish for $u \neq 0$. $P_{\rm c}(u)$ is the continuous part of the distribution and is non-zero for $u > 0$. In the effective medium approximation, the fluid flow conductivity is given by

$$\frac{1}{\sigma_{\rm eff}} = \frac{2}{\sigma_{\rm eff}} \frac{A}{A_0} + \int_0^\infty du \, \frac{2 P_{\rm c}(u)}{\sigma + \sigma_{\rm eff}} \tag{8}$$

where σ is given by (5) for an incompressible fluid, and by (6) for a compressible gas. Note that $\sigma_{\rm eff}$ occurs on both sides of (8) and (8) must be solved by iteration. Eq. (8) assumes isotropic roughness, but the theory can be extended to anisotropic roughness [36,37,41] (see also Appendix A).

When the contact area percolates, no fluid can flow at the interface, which corresponds to $\sigma_{\rm eff} = 0$. Multiplying (8) with $\sigma_{\rm eff}$ and taking the limit $\sigma_{\rm eff} \to 0$ gives $1 = 2A/A_0$ or $A/A_0 = 0.5$. Thus (8) predicts that the contact area percolates at $A/A_0 = 0.5$, but simulations show that for random roughness, percolation occurs at $A/A_0 \approx 0.42$ (see Ref. [15]). In Refs. [15,36,37,41] (see also Appendix A), it was shown how to modify the Bruggeman theory to give the correct percolation threshold [42].

In (8), the probability distribution $P_{\rm c}(u)$ is calculated using the Persson contact mechanics theory. For the torus-like geometry relevant here, the ensemble averaged fluid pressure $p_{\rm fluid}(x)$ and contact pressure $p_{\rm cont}(x)$ (the part of the total pressure resulting from the asperity contact area A) depend only on x.

In this case, for stationary flow, the continuity equation $\nabla \cdot \mathbf{J} = 0$ becomes

$$\frac{dJ_x}{dx} = \frac{d}{dx}\left(\sigma_{\rm eff} \frac{dp}{dx}\right) = 0$$

This equation is easy to integrate [34]: Let

$$S(x) = \int_0^x dx' \; \sigma_{\rm eff}^{-1}(p_{\rm cont}(x')) \tag{9}$$

then the leak rate is

$$\dot{Q} = \frac{L_y}{S(L_x)}(p_{\rm a} - p_{\rm b}) \tag{10}$$

where $L_y = 2\pi R$ is the length of the O-ring in the angular direction. For an incompressible fluid the leak rate $\dot{Q}$ is the volume of fluid per unit time (m^3/s) and for a compressible gas, it is the number of molecules per unit time (1/s).

The fluid pressure is

$$p_{\rm fluid}(x) = p_{\rm a} - (p_{\rm a} - p_{\rm b})\frac{S(x)}{S(L_x)} \tag{11}$$

The ensemble-averaged pressure acting on the rubber surface is

$$p_0(x) = p_{\rm cont}(x) + p_{\rm fluid}(x) \tag{12}$$

The pressure $p_0(x)$ arises from the macroscopic deformation of the rubber and was obtained from FEM simulations of the rubber stopper assuming smooth contact surfaces. The small change in interfacial separation induced by the fluid pressure has a negligible effect on $p_0(x)$, except for a small region near $x = 0$, where $p_0(x) \to 0$. In this region, the local surface separation exceeds the amplitude of the surface roughness, and the rubber surface is directly subjected to the fluid pressure $p_{\rm a}$. However, the leakage rate depends mainly on the central part of the nominal contact region, where the nominal pressure is highest. In this region, the change in surface separation is negligible compared to the overall compression of the stopper. The diameter of the rubber stopper is 0.4 mm larger than the inner diameter of the glass barrel. In the applications considered here, the surface separation at the critical constriction changes from ≈10 nm to ≈20 nm as the fluid pressure increases from zero to the highest value studied, which is negligible compared to the 0.2 mm radial compression. Hence, the nominal contact pressure $p_0(x)$ remains nearly unchanged by the small lift-off induced by the fluid pressure.

3. Leakage prediction using Persson contact mechanics software

A schematic representation of the system used in this study is shown in Fig. 2. The rubber stopper features three ribs with different shapes and heights that come into contact with the inner wall of the barrel. The present study focuses on the first rib, which is located closest to the fluid inside the barrel, since it plays the most critical role in preventing leakage. The aim is to assess the sealing performance of this specific

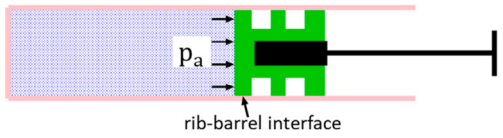

Fig. 2. Schematic representation of the studied system.

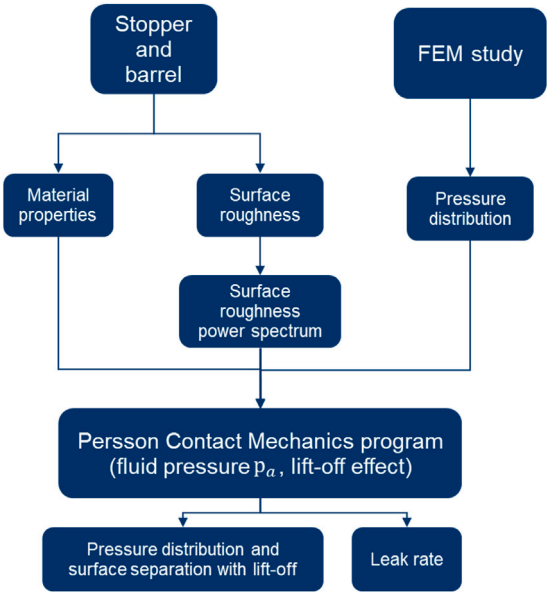

Fig. 3. General process for investigating leakage using MCM software.

interface. Therefore, this study concentrates on the interface between the first rib and the barrel, as indicated by the black arrow in the figure.

The general process for leakage prediction using MCM software is illustrated in Fig. 3.

Among the inputs required for the theoretical calculations, the surface roughness power spectral density (PSD) is the most critical. It is typically obtained from measured topography data using stylus or atomic force microscopy (AFM) techniques. Another key input is the pressure distribution within the rib-barrel interface. In this study, due to the complex geometry, the pressure distribution is asymmetric and was determined using FEM analysis. Additional input parameters include the temperature, fluid pressure, mechanical and rheological properties of the solid and fluid materials, such as the elastic modulus, Poisson's ratio, molecular mass and viscosity.

With all inputs prepared, the MCM software calculates important interfacial quantities such as contact pressure, surface separation, and leak rate, while accounting for the effect of lift-off (fluid-induced elastic deformation of the stopper).

3.1. Surface topography power spectra

When applying Persson contact mechanics theory to leakage analysis, it is assumed that surface roughness components with wavelengths larger than the nominal contact size do not significantly influence leakage. The roughness of interest is therefore limited to scales comparable to or smaller than the characteristic dimensions of the contact. To quantify this, we measured the topography of the rubber surface (on the first rib) using two engineering stylus instruments and an atomic force microscope (AFM). These methods have been shown to effectively characterize surface roughness across different length scales [43]. The surface of the glass tube is assumed to be smooth, as its roughness is much lower than that of the rubber surface.

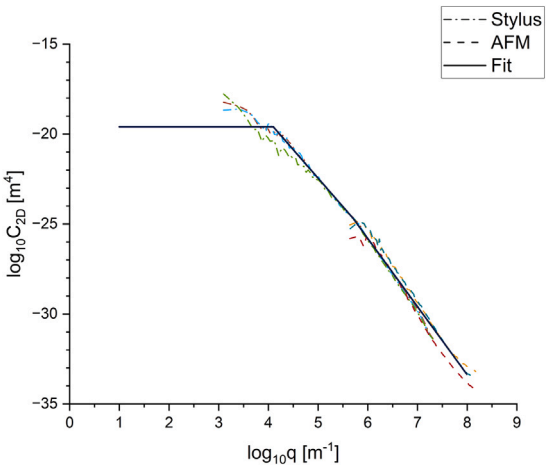

Fig. 4. 2D surface roughness power spectra calculated from stylus (dash-dot lines), AFM (dashed lines), and fitted PSD (solid line) used in calculations.

Two sets of engineering stylus measurements were performed: (a) using a Mitutoyo Portable Surface Roughness Measurement Surftest SJ-410 equipped with a diamond tip having a radius of curvature $R = 1$ μm and a tip-substrate repulsive force $F_N = 0.75$ mN. The step length (pixel size) was 0.5 μm, the scan length was $L = 2$ mm, and the tip speed was $v = 50$ μm/s; (b) using a Bruker Dektak XT, equipped with a diamond tip of radius $R = 0.7$ μm and a tip-substrate repulsive force $F_N = 1\times10^{-5}$ N. The scan length was $L = 3$ mm with a step resolution of 0.139 μm. The tip speed ranged from 33 to 44 μm/s. The Bruker Dektak was mounted on a vibration isolation table.

AFM measurements were conducted using a Bruker Dimension 3100 in tapping mode (amplitude modulation), equipped with an RSTESPA-300 probe having a tip radius of 8 nm. The two-dimensional scan resolution was 1024 × 1024 pixels over an area of 20 μm × 20 μm.

The topography data were processed using the MCM software to calculate the two-dimensional surface roughness PSD. The results are shown in Fig. 4. It can be seen that the stylus measurements (dash-dotted lines) and the AFM measurements (dashed lines) overlap well. Based on these data, a fitted PSD curve (solid line) was used for subsequent calculations. Note that, for technical reasons, a roll-off region was added to the fitted PSD at the wavenumber $q_r = 2\pi/L$, where L is the width of the contact region in the flow direction (i.e., the x-direction).

3.2. Contact pressures

The contact pressure in the rib-barrel interface was determined using FEM simulations, details are provided in Appendix B. The influence of fluid pressure p_a (relative to the atmosphere, i.e., $p_b = 0$) on the contact pressure was modeled by applying pressure to the mesh at the stopper–fluid interface [see Fig. 5(a)]. Seven distinct values of p_a were considered: 0, 0.069, 0.138, 0.207, 0.276, 0.345, and 0.414 MPa (corresponding to 0–60 psi in imperial units). Although it is impossible to calculate the leak rate at 0 MPa in the simulation, to obtain a finite value, the lowest p_a in all the simulations were set to 1 Pa.

In reality, the stoppers were not perfect cylinders but slightly oval. This effect was incorporated into the FEM model, resulting in non-uniform contact pressures along axial paths parallel to the stopper-barrel axis. Two axial paths, representing the nominal highest and lowest pressures, were selected for analysis. These paths served as the upper and lower bounds for the leakage rate.

Fig. 6 shows FEM-derived contact pressure distributions along the lowest pressure path at $p_a = 0$ and 0.414 MPa. The three distributions from left to right correspond to the three ribs on the stopper, with

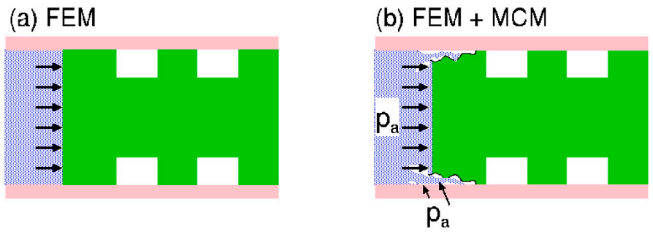

Fig. 5. (a) During fluid injection, the fluid pressure in the syringe compresses the rubber stopper, increasing the contact pressure at the rubber-barrel interface. This effect is included in the FEM analysis. (b) If open regions at the rubber-barrel interface are connected to the fluid via open channels, the fluid pressure will increase the average surface separation at the interface.

the stopper-fluid interface located on the far left. In the simulation, only the contact pressure distribution corresponding to the first rib (the first peak on the left) is used. It can be observed that applying fluid pressure to the stopper increases the contact pressure through elastic deformation.

The asymmetry observed in the pressure distribution in the first rib (peak on the left side of Fig. 6) originates from the actual geometry of the rubber stopper. The upper portions for the second and third ribs can be approximately described as symmetric circular arcs. In contrast, the first rib near the stopper head is inherently asymmetric: the side facing the fluid chamber forms a longer, gradual slope, whereas the opposite side is much steeper. This design ensures that when the internal liquid pressure increases, the deformation of the stopper promotes a corresponding increase in the local contact pressure, thereby enhancing the sealing performance.

In practice, the rubber stopper does not make full contact with the barrel due to surface roughness and the relatively small applied load. As a result, non-contact regions are present at the interface. If these regions are connected to the pressurized fluid inside the stopper, the fluid pressure at the interface will increase the average surface separation [see Fig. 5(b)]. This phenomenon is known as "lift-off". The MCM software calculations presented below incorporate this effect accurately.

At length scales larger than the characteristic contact dimensions, the deformation of the rubber ribs can be described using Hertzian contact mechanics, where the nominal pressure distribution is determined primarily by the overall geometry and applied load. At smaller scales, where surface roughness becomes significant for leakage, Persson contact mechanics theory is applied. In this multiscale framework, Hertzian mechanics defines the macroscopic contact pressure, while Persson theory accounts for the microscopic roughness effects that control leakage and lift-off behavior.

3.3. Determination of elastic modulus and fluid parameters

The stress–strain behavior of rubber materials is generally nonlinear, and this is accounted for in the FEM analysis. However, Persson contact mechanics assumes linear stress–strain behavior. One approach to obtain an effective modulus E_{eff} for use in Persson theory is to estimate the strain in the asperity contact regions and use the secant modulus corresponding to that strain from measured stress–strain curves in tension or compression.

Another approach, which we adopt here, is to fit the contact pressure distribution obtained from FEM to the distribution predicted by Hertzian contact theory, applied where the local contact is approximately Hertz-like. Assuming the material was linearly elastic, the Hertz theory would apply and an effective elastic modulus E_{eff} can be derived from the fit. This method has the advantage of producing a strain field that closely resembles that of asperity contact, involving not only compressive strains but also some shear deformation (included in the pressure distribution from FEM).

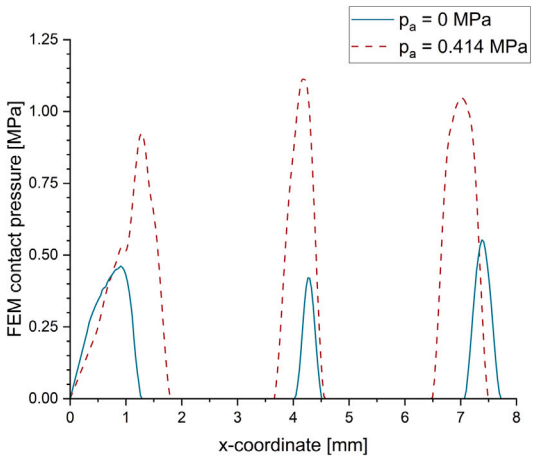

Fig. 6. FEM-simulated contact pressure distributions $p_0(x)$ along the lowest pressure path at fluid pressures p_a of 0 and 0.414 MPa. The three peaks represent the three ribs of the stopper. Only the pressure distribution of the first rib (the leftmost peak) was used in the simulation.

Thus, we determine the effective modulus E_{eff} by ensuring that the calculated Hertz contact pressure distribution closely matches the FEM results obtained using a full nonlinear material model. In this study, the Yeoh hyperelastic model was used in the FEM simulations [44] (See Appendix B). The second rib is approximated as having a half-cylinder cross-section, and the rib-barrel contact is assumed to follow Hertzian contact mechanics. From the radius of curvature of the rib and the contact width obtained from FEM, we chose E_{eff} such that the Hertzian maximum pressure matches the FEM prediction at the rib scale. This yields an effective modulus of $E_{\text{eff}} \approx 1.8$ MPa. We estimate that the compression of this rib (~35%) is also similar to the compression of the asperity contact regions, therefore, the result can be used on the first rib.

Using $E_{\text{eff}} \approx 1.8$ MPa and the surface roughness power spectrum shown in Fig. 4, and assuming that the contact area percolates when $A/A_0 \approx 0.42$, the nominal pressure at the percolation threshold is 0.64 MPa. This value can be compared to the maximum pressure at the first rib in the absence of fluid pressure, which is 0.46 MPa. This suggests that, in the absence of supplementary sealing mechanisms, leakage is likely to occur (see below).

This study investigates the leakage of air. To calculate the leak rate, both the viscosity and the effective mean free path of air molecules are required. As stated in Sec.2, if the mean free path is much larger than critical constriction along the gas flow channels, the gas flow is ballistic, and molecules will only collide with the wall. In the opposite limit, the motion is diffusive. The formalism used in this study accounts for both cases by interpolating between the diffusive and ballistic regimes [26].

In the present study, the viscosity of air is taken as $\eta_{\text{air}} \approx 1.8 \times 10^{-5}$ Pa s, and the mean free path is chosen as 60 nm.

4. Experimental setup

The test rig is shown in Fig. 7(a). It consists of several steel blocks and a Sony DK50NR5 displacement sensor with a resolution of 0.5 μm. The largest block weighs approximately 4.4 kg, and additional weights can be added to achieve different values of p_a. This method enables the consistent application of large loads, with a practical upper limit of approximately 20 kg when using lead blocks as the extra loading mass. The largest block includes a milled cylinder that pushes the rubber stopper into the glass barrel [see Fig. 7(b)]. During testing, a polymer spacer resembling a syringe piston is used to maintain proper compression and tension in the stopper, ensuring correct movement and avoiding tilting. The glass barrel of the prototype used for testing comes from the same production line as actual syringe barrels, with the only

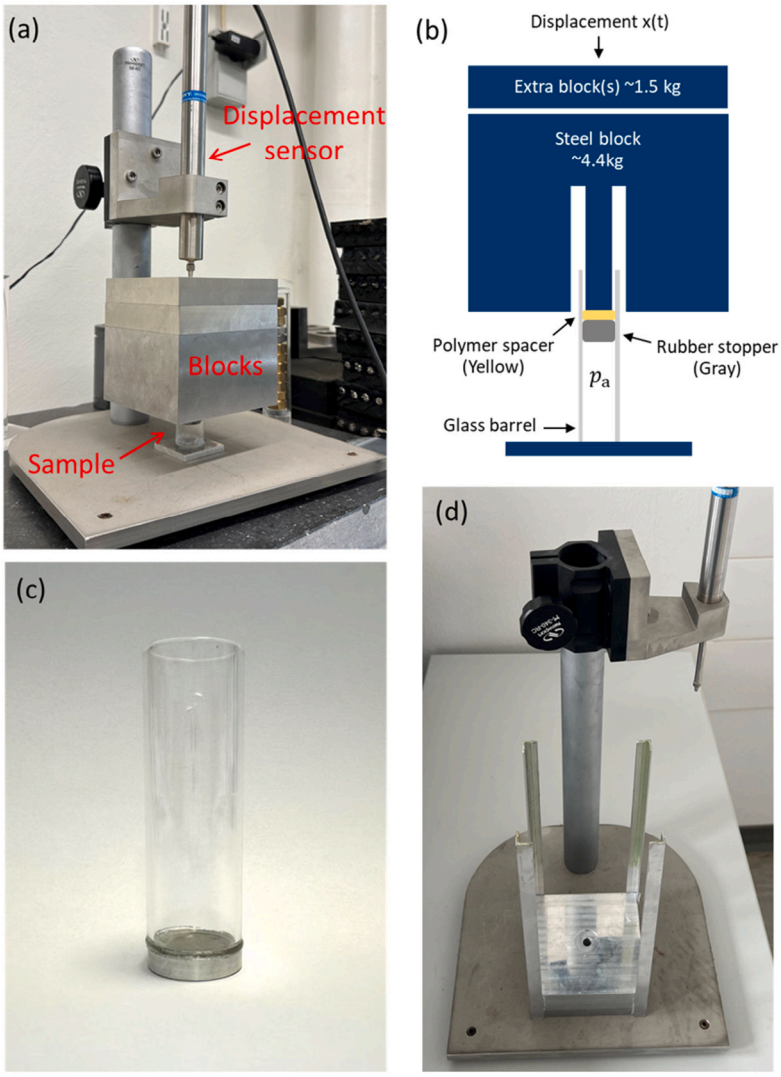

Fig. 7. (a) Experimental setup used in this study. (b) Schematic representation of the setup. (c) Glass barrel glued to a circular aluminum plate. (d) Base with rails on all four corners and a central recess to ensure proper alignment of the barrel and blocks.

difference being its shape. One end of the glass barrel is glued to a circular aluminum plate to ensure a tight seal [see Fig. 7(c)]. Finally, the barrel is positioned at the center of a base equipped with guiding rails at the corners [see Fig. 7(d)]. These rails guide the motion of the steel block, ensuring that the cylinder in the center of the block aligns precisely with the center of the glass barrel and pushes the stopper without contacting the barrel walls.

The basic principle of the setup is that by sealing the lower end of the barrel and applying a load to the stopper, any leakage is reflected by the displacement of the steel block over time under load. The volume of leaked air can be calculated by multiplying the measured displacement by the cross-sectional area of the barrel. This simple test method has been shown to be effective and provides results consistent with more complex techniques, such as helium leak testing [26].

Experimental measurements of air leakage were conducted using standard-size stoppers and glass barrels with an inner diameter of d = 19.05 mm. To match the simulation conditions, the experiments focused solely on leakage occurring at the first rib. To ensure this, cuts were made using a scalpel on the second and third ribs of the stopper, as shown in Fig. 8. These cuts were large enough to allow fluid (air) to pass through but not large enough to significantly affect the contact pressure.

The stoppers and barrels were siliconized at the factory. Therefore, leakage tests involving silicone oil were conducted first. To better

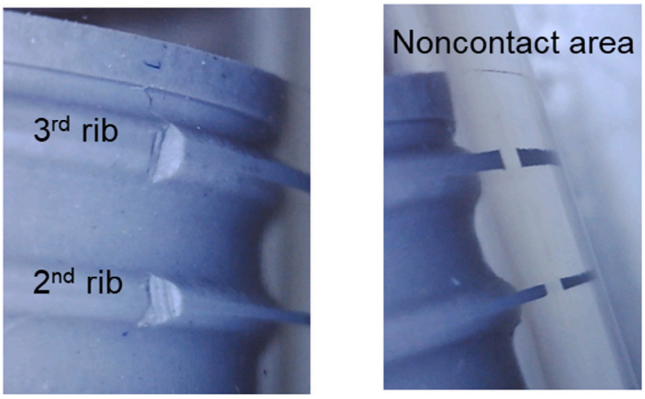

Fig. 8. Cuts and corresponding non-contact areas on the second and third ribs. The cuts were not large enough to significantly alter the contact pressure but were sufficient to allow air to pass through.

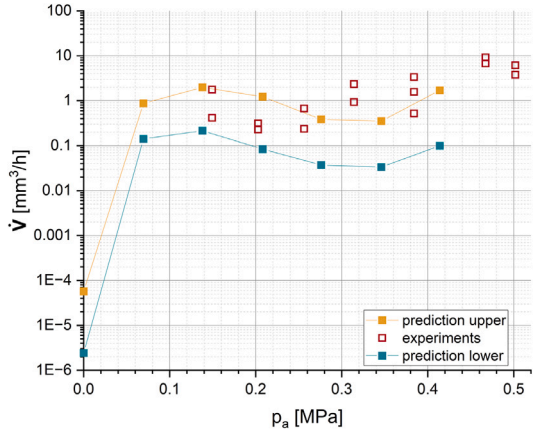

Fig. 9. Leak rate as a function of p_a. Experimental leak rates are reported as volumetric flow at ambient conditions. Comparison between simulation predictions (solid squares and lines) and experimental measurements (hollow squares) for clean syringes (nominally without silicone oil). The lowest p_a in the simulation was set to 1 Pa.

match the simulation conditions (i.e., dry contact between the stopper and barrel), subsequent tests were carried out after thoroughly cleaning both components with isopropyl alcohol to remove most of the silicone oil.

A key challenge in this experimental setup is estimating the internal pressure in the barrel, p_a, which is calculated as $p_a = F_N/A_0$, where F_N is the applied normal force and A_0 is the inner cross-sectional area of the barrel. Friction between the stopper and barrel, as well as between the steel block and guiding rails, may alter the actual value of F_N. In practice, some approximations are made: the guiding rails are lubricated with grease to minimize friction, which is then considered negligible. The friction between the stopper and barrel is measured to be on the order of a few newtons in the siliconized case and approximately 10 N under dry conditions. In both cases, the friction force is small compared to the applied load (≥44 N).

In total, approximately 20 randomly selected stoppers and 10 randomly selected glass barrels were tested. The combinations of stoppers and barrels were assembled in a standard (non-cleanroom) environment. After each trial, a visual inspection was performed to assess the condition of the components. This is important because contamination during assembly (e.g., dust particles or glass fragments) may alter the contact conditions and lead to anomalous test results, typically characterized by high leakage rates. In rare cases, such anomalies may also be due to defects in the stopper itself. If the glass barrel was determined to be in good condition, the stopper was replaced and the experiment was repeated. If not, a new barrel was used. The old barrel and, in some cases, the stoppers were cleaned with isopropyl alcohol and reused for non-siliconized tests.

In summary, all barrels and most stoppers underwent experiments with and without silicone oil. However, this does not imply that every stopper was tested in every barrel, as the combinations were relatively random.

5. Comparison between predictions and experimental results

Seven combinations of blocks were used in the test, resulting in p_a values ranging from 0.15 to 0.5 MPa. Note that 0.15 MPa corresponds to using only the largest block, which also defines the minimum p_a achievable in our setup.

For syringes with silicone oil, no leakage was observed. For nominally oil-free systems, leakage was detected and fell within the predicted range, as shown in Fig. 9. Both predicted and measured leak rates (volumetric flux) show an increasing trend (although non-monotonic) with fluid pressure p_a, which is consistent with the analysis of how lift-off influences the leak path size and resulting leak rate (discussed below).

The absence of leakage in siliconized systems can be attributed to the formation of capillary bridges and/or the time required to squeeze out the high-viscosity silicone oil. If silicone oil forms capillary bridges across the narrowest constrictions along the leakage flow paths, leakage can only occur if the fluid pressure p_a is sufficiently high to break these bridges. Given the good wetting properties of silicone oil for both rubber and glass surfaces, capillary bridges are expected to form when the surface separation is small.

The pressure required to break a capillary bridge is given by the Laplace pressure Δp, determined by the Young–Laplace equation [45,46]:

$$\Delta p = \gamma \left(\frac{1}{R_1} + \frac{1}{R_2} \right)$$

where R_1 and R_2 are the principal radii of curvature of the capillary bridge. In our experiments, the leaking fluid is air, and γ is the surface tension of silicone oil. If the syringe is filled with water, then γ refers to the surface tension of the silicone oil-water interface. Typically, $R_2 \gg R_1$, and $R_1 \approx u_c/2$, where u_c is the height of the critical junction. Therefore,

$$\Delta p \approx \frac{2\gamma}{u_c}$$

This relation implies that the pressure required to remove the capillary bridge is inversely proportional to the surface separation at the critical junctions. Hence, squeeze-out of silicone oil occurs only when $p_a > \Delta p$. For lower pressures, no leakage occurs if sufficient silicone oil exists to form capillary bridges.

More generally, if no leakage is observed within a given time period, it suggests either that p_a is too low to break the capillary bridges, or that the volume of silicone oil is sufficiently large that it is not squeezed out within the observation period. The time required for a complete squeeze-out depends on the silicone oil's viscosity, the pressure difference, and the length of the leak path. In siliconized systems, the presence of substantial amounts of silicone oil can significantly delay extrusion, preventing observable leakage during the test duration. Note that the viscosity of silicone oil (1 Pa s) is approximately 10^6 times higher than that of air.

The strength of capillary bridges in a siliconized system, or more generally the interfacial separation, is influenced by a complex interplay of factors. As the applied pressure p_a increases, the resulting deformation of the stopper tends to reduce the surface separation, increase the contact pressure and the real contact area, and consequently decrease leakage. As a result, the capillary bridges become stronger. However, an increase in p_a also enhances the lift-off effect, which acts in the opposite direction. These two effects counterbalance each other, leading to a non-monotonic dependence of the leak rate on p_a.

To remove silicone oil, some stoppers and barrels were cleaned with isopropyl alcohol. However, even after cleaning, traces of silicone oil may remain on the surface, or silicone oil present within the rubber may slowly diffuse back to the surface. Although the residual film thickness is likely on the nanometer scale, the separation at the critical junctions is also on the order of a few to tens of nanometers. If sufficiently small, these separations may still allow the formation of capillary bridges by residual silicone oil.

Another factor influencing leakage is the viscoelastic relaxation of the stopper material. Upon loading into the barrel, the stopper relaxes over time and becomes elastically softer (i.e., the effective modulus E decreases). This reduces the contact pressure but, at the same time, the softer rubber can more easily conform to the surface roughness. For a linearly elastic material, these two effects exactly compensate each other (discussed in next section), and the leak rate depends on the ratio p_0/E.

If the dominant surface roughness is on the barrel side (which is usually not the case), then during motion, the asperity contact regions

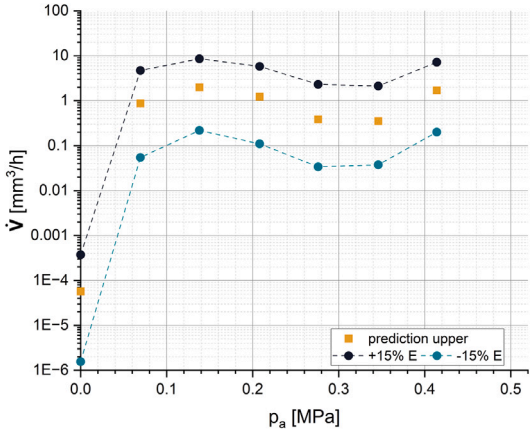

Fig. 10. Predicted leak rate with E varied by ±15% (blue and green dots with dashed lines).

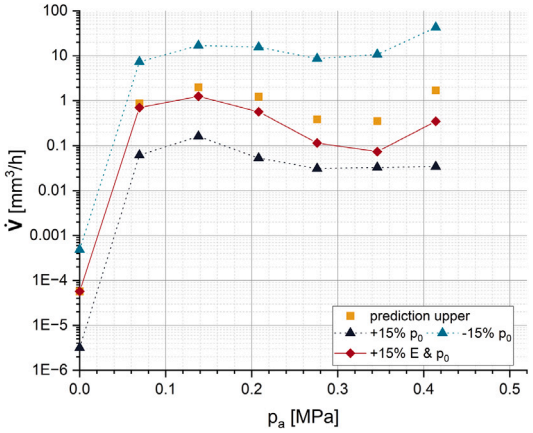

Fig. 11. Predicted leak rate with p_0 varied by ±15% (blue and green triangles with dotted lines), and both p_0 and E varied by +15% (red diamonds with line).

on the rubber side are continuously renewed. In this case, the rubber near the asperities remains elastically stiff, while it is soft on the macroscopic rib scale. As a result, the leak rate may increase with the time of stationary contact before sliding begins.

6. Elastic modulus and pressure sensitivity test

The sealing process is sensitive to the contact conditions, particularly the contact pressure p_0 and the elastic modulus E. When E is fixed, theory predicts that higher p_0 leads to smaller surface separation u, and thus a lower leak rate. Varying E gives a similar effect: under the same contact pressure, a higher E results in smaller asperity deformation, leading to a larger leak path and higher leak rate. This aligns with the common understanding that softer materials provide better sealing.

The dependency on p_0 and E becomes more critical when the contact approaches the percolation threshold, which depends on the stopper and barrel dimensions. To verify this, we performed a sensitivity test in simulation by varying p_0 and E and examining their influence on leakage for the path with the lowest contact pressure and highest leak rate.

We first used the original pressure distribution and varied the effective elastic modulus $E_{\text{eff}} = 1.8$ MPa by ±15%, resulting in $E^+ = 2.07$ MPa and $E^- = 1.53$ MPa. The results are shown in Fig. 10.

Next, using the original effective modulus $E_{\text{eff}} = 1.8$ MPa, we scaled the original contact pressure distribution $p_0(x)$ by ±15%. These results are presented in Fig. 11, along with an additional case where both p_0 and E are increased by 15%.

Fig. 12 summarizes all results from the sensitivity test.

The results obtained above lead to the following findings:

1. When p_0 is fixed, the leak rate increases with increasing E.
2. When E is fixed, the leak rate decreases with increasing p_0.
3. There is a nonlinear relationship between the leak rate $\dot{V}$ and the parameters p_0 and E across different fluid pressures p_a. At lower p_a, the influence of changes in p_0 and E on $\dot{V}$ is more pronounced than at higher p_a. For example, at $p_a = 0$ MPa, the difference in $\dot{V}$ between the prediction using $E = 1.8$ MPa and those using E^+ and E^- spans approximately one and two orders of magnitude, respectively. In contrast, at $p_a = 0.414$ MPa, the corresponding differences reduced to about 4 times higher and 1/9 lower, respectively. Similar behavior is observed when varying p_0. This sensitivity is attributed to the fact that near the percolation threshold, which corresponds to low p_a with negligible lift-off, the leak rate $\dot{V}$ is highly sensitive to small changes in the size of the leak paths, which depend on both p_0 and E. In contrast, under conditions where large interfacial separations are caused by high p_a, the effect of asperity deformation becomes less significant.
4. The errors caused by scaling E or p_0 highlight the importance of accurate FEM results when predicting leakage using Persson contact mechanics. In traditional FEM simulations, errors of 15% are common and often considered acceptable. However, our results show that such errors can lead to variations in predicted leak rates by several orders of magnitude.
5. Within the framework of linear elasticity, and assuming that p_a does not affect the contact pressure (i.e., lift-off effects are negligible), leakage becomes independent of E when compression is fixed (i.e., the geometry of the stopper and barrel remains unchanged). This is because increasing E raises the contact pressure, but simultaneously reduces the ability to conform to asperities in rubber. As a result, surface separation depends on the ratio p/E, making leakage independent of E [26]. This behavior is illustrated by the red diamonds and lines in Fig. 11, where both p_0 and E are increased by 15%. As seen, $\dot{V}$ remains unchanged until p_a becomes large enough to induce lift-off.
6. To improve sealing performance, reducing E and increasing p_0 yield similar effects across most p_a values, except at very high p_a (e.g., Fig. 12 at $p_a = 0.414$ MPa). Therefore, the most effective method for reducing leakage is to increase the contact pressure, for instance by tightening the seal.

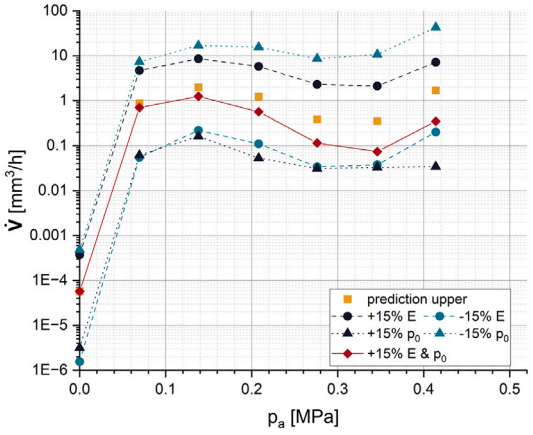

Fig. 12. Predicted leak rate with variations in p_0 and/or E.

7. Conclusion

In this study, we developed a new multiscale approach to investigate leakage at interfaces in a rubber stopper–glass barrel system. The approach combines macroscopic FEM simulations and Persson contact mechanics theory with measured surface roughness spectra, and relevant material properties to predict leakage.

FEM simulations were performed to capture the complex rib geometry of the stopper and the asymmetric contact pressure distribution along the interface. These calculations also included the influence of internal fluid pressure on the deformation of the stopper, which modifies the contact pressure profile. While FEM assumes smooth surfaces and full contact, in reality, fluid can penetrate non-contact regions due to surface roughness and increase the average surface separation under pressure, a phenomenon known as lift-off. This effect was incorporated into the calculations based on Persson theory, enabling accurate prediction of leakage rates.

The central input in Persson contact mechanics theory, the surface roughness of the rubber, was characterized using two engineering stylus instruments and AFM, providing reliable topography measurements across different length scales. These measurements were used to calculate the two-dimensional PSD of the surface.

Experimental leakage tests were conducted under controlled conditions, including both siliconized and cleaned (nominally dry) systems. Excellent agreement was obtained between the theoretical predictions and the experimental results for dry contacts, demonstrating the validity and predictive capability of the developed approach. For siliconized systems, no leakage was observed, which was attributed to the presence of capillary bridges formed by the silicone oil or to the delayed onset of leakage associated with squeeze-out of the silicone oil.

Additionally, a sensitivity analysis was carried out to investigate the influence of the elastic modulus $E_{\rm eff}$ and contact pressure $p_0(x)$ on leakage. Results demonstrated that both parameters strongly affect leakage rates, particularly near the percolation threshold. The analysis revealed that small deviations in input parameters, such as those typically considered acceptable in FEM simulations, can lead to large variations in the predicted leakage rate. This highlights the importance of accurate input data, including realistic rheological models of the rubber, precise geometric representation of the stopper and barrel, and reliable experimental characterization of surface roughness and material properties, when applying contact mechanics models for seal design and evaluation.

Overall, this study enhances the understanding of the interplay between surface roughness, material properties, and sealing performance. It also reveals the beneficial effect of silicone oil at the interface in improving sealing performance. Moreover, the developed approach provides a predictive tool to support the design and optimization of reliable sealing systems in pharmaceutical and engineering applications.

CRediT authorship contribution statement

R. Xu: Data curation, Formal analysis, Funding acquisition, Investigation, Methodology, Project administration, Resources, Software, Supervision, Validation, Visualization, Writing – original draft, Writing – review & editing. **L. Gil:** Conceptualization, Investigation, Project administration, Resources, Supervision, Validation, Visualization, Writing – review & editing. **J. Singer:** Conceptualization, Data curation, Investigation, Project administration, Supervision, Validation, Visualization, Writing – review & editing. **L. Gontard:** Data curation, Investigation, Methodology. **W. Leverd:** Conceptualization, Formal analysis, Funding acquisition, Project administration, Resources, Supervision, Validation, Visualization. **B.N.J. Persson:** Conceptualization, Data curation, Formal analysis, Funding acquisition, Investigation, Methodology, Project administration, Resources, Software, Supervision, Validation, Visualization, Writing – original draft, Writing – review & editing.

Declaration of competing interest

The authors declare that they have no known competing financial interests or personal relationships that could have appeared to influence the work reported in this paper.

Appendix A. Fluid flow conductivity

We consider the flow of a fluid (liquid or gas) at the interface between two elastic solids with anisotropic roughness characterized by the Tripp number γ, which is the ratio between the average size of the asperities (and valleys) in the x and y directions (see Fig. 13). Some of the results presented below were derived in Refs. [36,41,47] for the flow of incompressible fluids but are extended here to gas flow in the ballistic limit.

For this case, in a coordinate system where the flow conductivity tensor is diagonal, the effective medium theory predicts:

$$\frac{1}{\sigma_x} = \left\langle \frac{1+(n-1)\gamma^*}{\sigma(u)+\gamma^*(n-1)\sigma_x} \right\rangle \tag{A.1}$$

$$\frac{1}{\sigma_y} = \left\langle \frac{1+(n-1)(1/\gamma^*)}{\sigma(u)+(1/\gamma^*)(n-1)\sigma_y} \right\rangle \tag{A.2}$$

where the effective Tripp number $\gamma^* = (\sigma_y/\sigma_x)^{1/2}\gamma$. Here, $\langle..\rangle$ denotes averaging over the probability distribution $P(u)$ of the interfacial separation, e.g.,

$$\langle f(u)\rangle = \int_0^\infty P(u) f(u)$$

In (A.1) and (A.2), the number n appears, which in the Bruggeman effective medium theory corresponds to the dimension D of the fluid flow problem. For the interfacial flow considered here, $D = 2$. However, using $n = 2$ results in percolation of the contact area when $A/A_0 = 0.5$, while experiments show that for randomly rough surfaces, percolation occurs at $A/A_0 \approx 0.42$. This discrepancy can be accounted for by using a dimension n slightly less than 2 [see (A.6) below, which gives $n \approx 1.75$]. We have found that using this value of n yields leakage rates in almost perfect agreement with first-principles calculations of the fluid flow, which are feasible for small systems with roughness extending over approximately two decades in length scale [15].

If A/A_0 denotes the normalized contact area, then we can write:

$$P(u) = \frac{A}{A_0}\delta(u) + P_{\rm c}(u) \tag{A.3}$$

where $P_{\rm c}(u)$ is the contribution from the surface region where $u > 0$. Substituting (A.3) into (A.1) and (A.2), and using that $\sigma(0) = 0$, gives:

$$\frac{1}{\sigma_x} = \frac{A_{\rm p}}{A_0}\left[\frac{1+(n-1)\gamma^*}{\gamma^*(n-1)\sigma_x}\right] + \int_0^\infty du\ \frac{1+(n-1)\gamma^*}{\sigma(u)+\gamma^*(n-1)\sigma_x} P(u) \tag{A.4}$$

$$\frac{1}{\sigma_y} = \frac{A_{\rm p}}{A_0}\left[\frac{1+(n-1)(1/\gamma^*)}{(1/\gamma^*)(n-1)\sigma_y}\right] + \int_0^\infty du\ \frac{1+(n-1)(1/\gamma^*)}{\sigma(u)+(1/\gamma^*)(n-1)\sigma_y} P(u) \tag{A.5}$$

When the contact area percolates, no fluid can flow at the interface and the flow conductivity vanishes. Note that for a surface with random roughness, both σ_x and σ_y vanish when the contact area percolates. This is trivially true for a system with isotropic roughness, but also holds for a system with anisotropic roughness.

This can be understood in the limiting case where the anisotropic roughness is obtained by stretching in the x-direction a system with isotropic roughness. If the contact area percolates before the stretching, it must also percolate after the stretching. And if it does not percolate before stretching, it cannot percolate afterward.

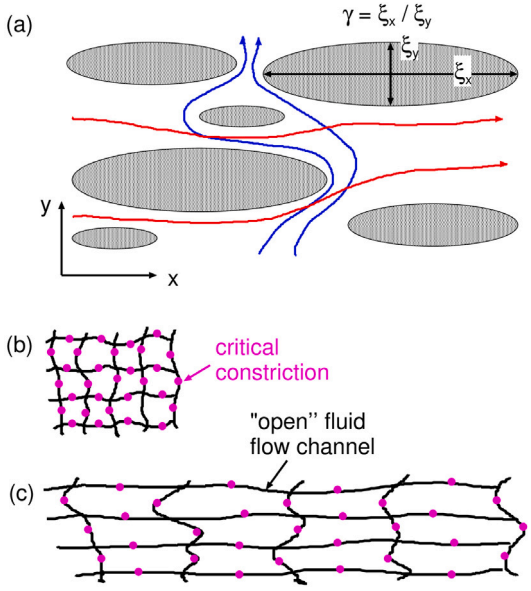

Fig. 13. (a) Fluid flow in a contact with anisotropic roughness with Tripp number $\gamma = 4$ (schematic). The fluid flow conductivity in the x-direction is larger than that in the y-direction. (b) Percolating (open) fluid flow channels (black lines) with narrow (critical) constrictions (pink dots), across which most of the fluid pressure drop occurs. (c) If the system in (b) is stretched by a factor λ (here $\lambda = 4$) in the x-direction, the number of fluid flow channels per unit area in the x-direction remains unchanged, but the concentration of critical junctions along these channels decreases by a factor $1/\lambda$, which increases the flow conductivity σ_x by a factor λ. After stretching, the number of fluid flow channels per unit surface area in the y-direction decreases by a factor $1/\lambda$, while the concentration of critical constrictions along these channels remains unchanged. As a result, the flow conductivity σ_y decreases by a factor $1/\lambda$. Therefore, for the stretched system, $\sigma_x = \gamma^2\sigma_y$.

From (A.4) and (A.5), as $\sigma_x \to 0$ and $\sigma_y \to 0$, we get:

$$\frac{A_p}{A_0}\left[\frac{1+(n-1)\gamma^*}{\gamma^*(n-1)}\right] = 1$$

$$\frac{A_p}{A_0}\left[\frac{1+(n-1)(1/\gamma^*)}{(1/\gamma^*)(n-1)}\right] = 1$$

It follows that $\gamma^* = 1$ and

$$\frac{A_p}{A_0}\left[\frac{1+(n-1)}{n-1}\right] = 1$$

or

$$n = \frac{1}{1-A_p/A_0} \tag{A.6}$$

The condition $\gamma^* = 1$ implies that $\sigma_x = \gamma^2\sigma_y$, so that close to the percolation threshold, we expect the fluid current in the x-direction to be γ^2 times higher than in the y-direction. The physical reason why the flow current is larger in the x-direction than in the y-direction is illustrated in Fig. 13(b,c).

The flow conductivity can be obtained by numerical integration and iteration from (A.1) and (A.2). However, for large interfacial separation $\bar{u}$, this is not convenient, and σ_x and σ_y for large $\bar{u}$ can instead be determined analytically. The result depends on $\sigma(u)$. For liquids, $\sigma(u) \sim u^3$ [see (5)], and for this case, the asymptotic large-u form of the flow conductivity was derived in Ref. [47].

For ballistic gas flow, $\sigma(u) \sim u^2$ [see the second term in (6)], and the asymptotic large-u form of the flow conductivity can be obtained as follows. For ballistic gas flow:

$$\sigma(u) = \frac{\bar{v}u^2}{2k_BT}$$

which we write as αu^2 for simplicity. If $\bar{u} = \langle u\rangle$ is the ensemble-averaged surface separation (i.e., the surface separation after averaging over the roughness), we write $u = \bar{u} + u_1$ where $\langle u_1\rangle = 0$. For large surface separation, there is no contact between the surfaces, and the surface roughness is not elastically deformed; hence, we expect $\langle u_1^2\rangle$ to equal the mean square roughness h_{rms}^2 of the undeformed surface. Defining $\bar{\sigma} = \alpha\bar{u}^2$, we get:

$$\sigma = \alpha\left(\bar{u}+u_1\right)^2 = \bar{\sigma} + 2\alpha\bar{u}u_1 + \alpha u_1^2 = \bar{\sigma}\left(1+2\epsilon+\epsilon^2\right).$$

Here, $\epsilon = u_1/\bar{u}$ is small when $\bar{u}$ is large, with $\langle\epsilon\rangle = 0$ and $\langle\epsilon^2\rangle = h_{rms}^2/\bar{u}^2$.

Writing $\sigma_x/\bar{\sigma} = y$, then (A.1) becomes:

$$\frac{1}{y} = \left\langle \frac{1+(n-1)\gamma^*}{1+2\epsilon+\epsilon^2+\gamma^*(n-1)y}\right\rangle$$

We compute y to second order in ϵ (the first-order term vanishes). Writing $\mu = 1/[1+\gamma^*(n-1)y]$, we get:

$$\frac{1}{y} = [1+(n-1)\gamma^*]\mu\left\langle\frac{1}{1+2\epsilon\mu+\epsilon^2\mu}\right\rangle$$

Expanding to second order in ϵ and using $\langle\epsilon\rangle = 0$:

$$\frac{1}{y} = [1+(n-1)\gamma^*]\mu\left[1-\langle\epsilon^2\rangle\left(4\mu^2-\mu\right)\right]$$

or

$$\frac{1}{y} = \left[\frac{1+(n-1)\gamma^*}{1+(n-1)\gamma^*y}\right]\left[1-\langle\epsilon^2\rangle\left(4\mu^2-\mu\right)\right] \tag{A.7}$$

This equation shows that to zeroth order in ϵ, $y = 1$ or $\sigma_x = \bar{\sigma}$, as expected. Writing $y = 1 + a\langle\epsilon^2\rangle$, we get to second order:

$$\frac{1+(n-1)\gamma^*}{1+(n-1)\gamma^*y} = 1-(n-1)\gamma^*a\mu_1\langle\epsilon^2\rangle$$

where $\mu_1 = 1/[1+(n-1)\gamma^*] = \mu$ at $y = 1$. Using this in (A.7):

$$1-a\langle\epsilon^2\rangle = \left[1-(n-1)\gamma^*a\mu_1\langle\epsilon^2\rangle\right]\left[1-\langle\epsilon^2\rangle(4\mu_1^2-\mu_1)\right]$$

or

$$a\left[-1+(n-1)\gamma^*\mu_1\right] = 4\mu_1^2-\mu_1$$

so

$$a = 1-4\mu_1 = \frac{(n-1)\gamma^*-3}{1+(n-1)\gamma^*}$$

Hence,

$$\sigma_x = \bar{\sigma}\left(1+\left[\frac{(n-1)\gamma^*-3}{(n-1)\gamma^*+1}\right]\langle\epsilon^2\rangle\right) \tag{A.8}$$

A similar expression with γ^* replaced by $1/\gamma^*$ results for σ_y. Since both σ_x and σ_y are equal to $\bar{\sigma}$ to zeroth order in ϵ, we can replace $\gamma^* = (\sigma_y/\sigma_x)^{1/2}\gamma$ with γ in (A.8) and the corresponding equation for σ_y. Using this and replacing $\langle\epsilon^2\rangle$ with $h_{rms}^2/\bar{u}^2$ gives:

$$\sigma_x = \bar{\sigma}\left(1+\left[\frac{(n-1)\gamma-3}{(n-1)\gamma+1}\right]\frac{h_{rms}^2}{\bar{u}^2}\right) \tag{A.9}$$

$$\sigma_y = \bar{\sigma}\left(1+\left[\frac{(n-1)/\gamma-3}{(n-1)/\gamma+1}\right]\frac{h_{rms}^2}{\bar{u}^2}\right) \tag{A.10}$$

For the case of a liquid, $\sigma \sim u^3$ [see (5)], and a similar derivation gives the asymptotic (large $\bar{u}$) relations:

$$\sigma_x = \bar{\sigma}\left(1+\left[\frac{3[(n-1)\gamma-2]}{(n-1)\gamma+1}\right]\frac{h_{rms}^2}{\bar{u}^2}\right) \tag{A.11}$$

$$\sigma_y = \bar{\sigma}\left(1+\left[\frac{3[(n-1)/\gamma-2]}{(n-1)/\gamma+1}\right]\frac{h_{rms}^2}{\bar{u}^2}\right) \tag{A.12}$$

The expression for σ_x was derived in Appendix A of Ref. [47] for the case $n = 2$ (a misprint in the derivation was overlooked during proofreading, but the final result is correctly stated).

Appendix B. FEM simulation

The actual rubber stopper is slightly oval rather than perfectly circular. This real geometry was incorporated into the FEM simulations, which explains the non-uniform contact pressure observed along axial paths parallel to the barrel axis.

All simulations were performed using Abaqus. The rubber material was modeled with a hyperelastic constitutive law calibrated from tensile and compressive measurements. The Yeoh hyperelastic model [44] was adopted where the elastic (strain) energy is given by

$$W(\bar{I}_1, J) = \sum_{i=1}^{N} C_{i0}\,(\bar{I}_1 - 3)^i + \sum_{i=1}^{N} \frac{1}{D_i}\,(J-1)^{2i}, \tag{B.1}$$

with

$$\bar{I}_1 = J^{-2/3} I_1, \qquad I_1 = \lambda_1^2 + \lambda_2^2 + \lambda_3^2, \qquad J = \lambda_1 \lambda_2 \lambda_3.$$

In this equation $\lambda_1 = L_1/L_0$ is the extension ratio in the x-direction, and similar for λ_2 and λ_3. For an incompressible material the volume does not change so that $L_1 L_2 L_3 = L_0^3$ or $\lambda_1 \lambda_2 \lambda_3 = 1$.

The first summation term represents the isochoric contribution, while the second term corresponds to the volumetric penalty. In Abaqus, $N = 3$, and the material coefficients used are:

$$C_{10} = 59.59788609, \qquad C_{20} = 0.494230192$$

$$C_{30} = 0, \qquad D_1 = 3.39386 \times 10^{-5}.$$

By using a very small value for D_1 minimization of the free energy (B.1) will result in $J \approx 1$, so the material is treated as (nearly) incompressible, and the terms D_2 and D_3 are deactivated.

Data availability

Data will be made available on request.

References

[1] Persson BNJ. On the fractal dimension of rough surfaces. Tribol Lett 2014;54:99–106.
[2] Ranganath Nayak P. Random process model of rough surfaces. 1971.
[3] Aghababaei Ramin, Brodsky Emily E, Molinari Jean-François, Chandrasekar Srinivasan. How roughness emerges on natural and engineered surfaces. MRS Bull 2022;47(12):1229–36.
[4] Greenwood James A, Pl Williamson JB. Contact of nominally flat surfaces. Proc R Soc Lond Ser A. Math Phys Sci 1966;295(1442):300–19.
[5] Persson BNJ. Theory of rubber friction and contact mechanics. J Chem Phys 2001;115(8):3840–61.
[6] Persson BNJ. Adhesion between an elastic body and a randomly rough hard surface. Eur Phys J E 2002;8:385–401.
[7] Persson BNJ. Contact mechanics for randomly rough surfaces. Surf Sci Rep 2006;61(4):201–27.
[8] Persson BNJ. Relation between interfacial separation and load: a general theory of contact mechanics. Phys Rev Lett 2007;99(12):125502.
[9] Persson BNJ. On the elastic energy and stress correlation in the contact between elastic solids with randomly rough surfaces. J Phys Condens Matter 2008;20(31).
[10] Yang C, Persson BNJ. Contact mechanics: contact area and interfacial separation from small contact to full contact. J Phys: Condens Matter 2008;20(21):215214.
[11] Almqvist Andreas, Campana C, Prodanov N, Persson BNJ. Interfacial separation between elastic solids with randomly rough surfaces: comparison between theory and numerical techniques. J Mech Phys Solids 2011;59(11):2355–69.
[12] Bush AW, Gibson RD, Thomas TR. The elastic contact of a rough surface. Wear 1975;35(1):87–111.
[13] Chang WR, Etsion I, Bogy DB. An elastic–plastic model for the contact of rough surfaces. J Tribol 1987.
[14] Carbone G, Bottiglione F. Contact mechanics of rough surfaces: a comparison between theories. Meccanica 2011;46:557–65.
[15] Dapp Wolf B, Lücke Andreas, Persson Bo NJ, Müser Martin H. Self-affine elastic contacts: percolation and leakage. Phys Rev Lett 2012;108(24):244301.
[16] Persson BNJ, Yang C. Theory of the leak-rate of seals. J Phys: Condens Matter 2008;20(31):315011.
[17] Lorenz B, Persson BNJ. On the dependence of the leak rate of seals on the skewness of the surface height probability distribution. Europhys Lett 2010;90(3):38002.
[18] Dapp W, Müser M. Fluid leakage near the percolation threshold. Sci Rep 2016;6:19513.
[19] Persson BNJ. Leakage of metallic seals: role of plastic deformations. Tribol Lett 2016;63:1–6.
[20] Fischer FJ, Schmitz K, Tiwari A, Persson BNJ. Fluid leakage in metallic seals. Tribol Lett 2020;68(4):125.
[21] Fischer Felix, Murrenhoff Hubertus, Schmitz Katharina. Influence of normal force in metallic sealing. Eng Rep 2021;3(10):e12399.
[22] Tiwari Avinash, Dorogin Leonid, Tahir Muhammed, Stöckelhuber Klaus Werner, Heinrich Gert, Espallargas Nuria, Persson Bo NJ. Rubber contact mechanics: adhesion, friction and leakage of seals. Soft Matter 2017;13(48):9103–21.
[23] Akulichev AG, Echtermeyer AT, Persson BNJ. Interfacial leakage of elastomer seals at low temperatures. Int J Press Vessels Pip 2018;160:14–23.
[24] Persson BNJ. Fluid leakage in static rubber seals. Tribol Lett 2022;70(2):31.
[25] Rodriguez Nestor, Tiwari Avinash, Persson BNJ. Air leakage in seals with application to syringes. Appl Surf Sci Adv 2022;8:100222.
[26] Huon Carine, Tiwari Avinash, Rotella Cinzia, Mangiagalli Paolo, Persson BNJ. Air, helium and water leakage in rubber O-ring seals with application to syringes. Tribol Lett 2022;70(2):35.
[27] Fischer Felix, Bady Dariush, Schmitz Katharina. Leakage of metallic ball seat valves with anisotropic surfaces. Chem Eng Technol 2023;46(1):102–9.
[28] Bauer Niklas, Schmitz Katharina. Influence of manufacturing tolerances on the behavior of pneumatic seals using EHL simulations. Tribol Und Schmier 2022;69(5+6):62–9.
[29] Peng Chao, Ouyang Xiaoping, Schmitz Katharina, Wang Wei, Guo Shengrong, Yang Huayong. Investigation of the tribological performance of reciprocating seals in a wide temperature range. Proc Inst Mech Eng Part J: J Eng Tribol 2021;235(11):2396–414.
[30] Wang Jiehao, Li Jing, Bauer Niklas, Schmitz Katharina. Numerical study of leakage rate in reciprocating seal with non-Gaussian topography characteristics using percolation mechanism. Tribol Int 2024;199:109955.
[31] Persson BNJ. Side-leakage of face mask. Eur Phys J E 2021;44(6):75.
[32] Lorenz B, Persson BNJ. Leak rate of seals: Comparison of theory with experiment. EPL 2009;86(4).
[33] Lorenz B, Persson BNJ. Leak-rate of seals: effective medium theory and comparison with experiment. 2009.
[34] Lorenz B, Persson BNJ. Time-dependent fluid squeeze-out between solids with rough surfaces. Eur Phys J E 2010;32:281–90.
[35] Lorenz B, Rodriguez N, Mangiagalli P, Persson BNJ. Role of hydrophobicity on interfacial fluid flow: Theory and some applications. Eur Phys J E 2014;37:1–14.
[36] Persson BNJ. Comments on the theory of fluid flow between solids with anisotropic roughness. Tribol Lett 2021;69(1).
[37] Wang Anle, Müser Martin H. Percolation and Reynolds flow in elastic contacts of isotropic and anisotropic, randomly rough surfaces. Tribol Lett 2021;69(1).
[38] Scaraggi M. The friction of sliding wet textured surfaces: the Bruggeman effective medium approach revisited. Proc R Soc A: Math Phys Eng Sci 2015;471(2183):20140739.
[39] Bottiglione F, Carbone G, Mangialardi L, Mantriota G. Leakage mechanism in flat seals. J Appl Phys 2009;106(10).
[40] Bruggeman DAG. Berechnung verschiedener physikalischer konstanten von heterogenen substanzen. I. Dielektrizitätskonstanten und leitfähigkeiten der mischkörper aus isotropen substanzen. Ann Phys, Lpz 1935;416(7):636–64.
[41] Persson BNJ. Interfacial fluid flow for systems with anisotropic roughness. Eur Phys J E 2020;43(5):25.
[42] The equation for how to obtain the correct percolation limit given in Ref. [41] contained a misprint which was pointed out by Wang et al (Ref. [37]) and was corrected in Ref. [36].
[43] Rodriguez N, Gontard L, Ma C, Xu R, Persson BNJ. On how to determine surface roughness power spectra. Tribol Lett 2025;73(1).
[44] Yeoh OH. Some forms of the strain energy function for rubber. Rubber Chem Technol 1993;66(5):754–71.
[45] Adamson Arthur W, Gast Alice Petry. Physical chemistry of surfaces. vol. 150, New York; 1967.
[46] Kralchevsky PAAN, Nagayama Kuniaki. Particles at fluid interfaces and membranes: attachment of colloid particles and proteins to interfaces and formation of two-dimensional arrays. Elsevier; 2001.
[47] Persson BNJ, Prodanov N, Krick BA, Rodriguez N, Mulakaluri N, Sawyer WG, Mangiagalli P. Elastic contact mechanics: percolation of the contact area and fluid squeeze-out. Eur Phys J E 2012;35:1–17.